

Decentralized Multi-Robot Obstacle Detection and Tracking in a Maritime Scenario

Muhammad Farhan Ahmed¹, Vincent Frémont¹

Abstract— Autonomous aerial-surface robot teams are promising for maritime monitoring. Robust deployment requires reliable perception over reflective water and scalable coordination under limited communication. We present a decentralized multi-robot framework for detecting and tracking floating containers using multiple UAVs cooperating with an autonomous surface vessel. Each UAV performs YOLOv8 and stereo-disparity based visual detection, then tracks targets with per-object EKFs using uncertainty-aware data association. Compact track summaries are exchanged and fused conservatively via covariance intersection, ensuring consistency under unknown correlations. An information-driven assignment module allocates targets and selects UAV hover viewpoints by trading expected uncertainty reduction against travel effort and safety separation. Simulation results in a maritime scenario demonstrate improved coverage, localization accuracy, and tracking consistency, while maintaining modest communication requirements

I. INTRODUCTION

Teams of aerial and surface robots are increasingly used in maritime missions, including infrastructure inspection, environmental monitoring, and search-and-rescue. Operating over water, however, remains challenging: specular reflections, waves, and low-texture regions degrade vision, while long distances and intermittent line-of-sight impose tight communication and coordination constraints. Reliable deployment, therefore, requires accurate state estimation, robust object perception, and scalable multi-robot cooperation under limited bandwidth [1].

In this article, we present a decentralized multi-robot perception framework for detecting and tracking floating containers using multiple UAVs cooperating with a autonomous surface vessel (Aquabot). Each agent runs an onboard EKF localization in a shared world frame. UAVs perform YOLOv8-based detection and exploit stereo disparity for 3D detection. Each container is tracked locally with an EKF and Mahalanobis-gated updates. Robots exchange compact track summaries that are fused conservatively via covariance intersection (CI), ensuring consistency in the presence of unknown cross-correlations. Building on the fused tracks, we introduce an information-driven allocator that assigns targets and selects UAV hover viewpoints by trading expected uncertainty reduction against travel effort and inter-drone separation. UAVs switch between SURVEILLANCE and

TRACKING modes to focus sensing resources on the most informative targets.

Our main contributions are: (i) A decentralized pipeline for maritime multi-robot detection and tracking that combines stereo perception, EKF-based tracking, and CI-based fusion; (ii) An information-driven target allocation method that prioritizes targets by expected uncertainty reduction while enforcing safety and load constraints; and (iii) A mode-switching and hover viewpoint selection strategy that maintains observability and improves coverage and tracking accuracy.

This paper is organized as follows: Section II reviews related work, decentralized fusion, and information-aware assignment. Section III presents the proposed method, Section IV presents the simulation setup along with the results. Finally, Section V concludes the paper by summarizing the main contributions and outlining directions for future work.

II. RELATED WORK

A. Maritime Visual Detection

Recent real-time detectors have rapidly emphasized end-to-end training and stronger latency-accuracy trade-offs [2]. Maritime UAV imagery introduces a strong domain shift due to specular reflections, haze, low horizon contrast, and scale variation; therefore, recent works emphasize maritime-specific training and adaptation for robustness [3], [4]. Public benchmarks that support systematic evaluation in open-water conditions are also increasingly used (e.g., SeaDronesSee and related recent maritime vision challenges) [5], [6], [7], [8].

In our pipeline, we couple detector inputs with stereo disparity to obtain metric observations, improving association robustness under occlusion. For dense stereo estimation, we build on modern learning-based stereo matching that is robust in challenging textures and long-range settings [9].

B. Multi-Object Tracking

Tracking-by-detection pipelines increasingly rely on stronger association logic and more stable motion modeling, with recent baselines improving robustness in crowded scenes and under detection noise [10]. For 3D settings, simple Bayesian filtering can still be competitive when measurements are metric and uncertainty is well modeled [11]. In maritime tracking specifically, lightweight trackers remain attractive due to their stability under intermittent observations and modest compute constraints [12]. Recent maritime benchmarks and datasets further highlight failure modes caused by glare, wake effects, and fast appearance changes

¹Muhammad Farhan Ahmed and Vincent Frémont are with LS2N, Ecole Centrale de Nantes (ECN), 1 Rue de la Noë, 44300 Nantes, France. Muhammad.Ahmed@ec-nantes.fr, vincent.fremont@ec-nantes.fr

[13]. Motivated by these findings, we adopt independent EKFs with Mahalanobis gating and perform conservative inter-robot fusion to avoid overconfident cross-agent track updates.

C. Decentralized Fusion

Multi-robot estimation must address unknown inter-robot correlations caused by shared priors, repeated communications, or common sensing. Recent work on consistent distributed cooperative localization continues to emphasize conservative fusion mechanisms and estimator consistency under realistic networking constraints [14], [15], [16]. In this spirit, we employ track-level CI with gating to prevent fusing unrelated hypotheses and to remain robust under intermittent communication [17].

D. Assignment and Task Allocation

Dynamic multi-robot task allocation (MRTA) has seen renewed attention with modern optimization-based formulations and scalable solvers. Recent surveys and reviews summarize optimization techniques and provide practical guidance on modeling costs, constraints, and dynamics in MRTA [18]. For dynamic settings, recent work studies online and formal optimization approaches that better capture feasibility and evolving task demands [19], [20]. In our maritime perception setting, we adopt a capacitated min-cost flow formulation and define costs using expected information gain, travel effort, safety separation, and assignment stickiness.

III. METHODOLOGY

Existing maritime perception pipelines often rely on 2D-only detections and standard online association, which can become brittle over reflective water, low contrast, and intermittent visibility, leading to unstable measurements and frequent track fragmentation [21], [22], [23]. In multi-robot settings, centralized fusion further increases bandwidth dependence and can become inconsistent when track estimates are correlated through shared priors or common observations; naïve fusion may then become over-confident [24], [25]. We address these limitations by lifting detections to metric 3D using stereo disparity, tracking each target with lightweight EKFs, and performing conservative decentralized fusion via covariance intersection, coupled with information-driven assignment to focus sensing on the most uncertain targets.

We present a multi-UAV obstacle detection and tracking method based on target information gain in a marine environment. We consider multiple UAVs and a surface vessel (Aquabot) operating in a shared ENU (East–North–Up) world frame. UAVs detect floating containers in SURVEILLANCE mode using YOLOv8 with stereo disparity, estimate their poses and track container states with onboard EKFs, and share compact track summaries with the Aquabot, which fuses them via CI. A capacitated min-cost flow (CMCF) allocator assigns each UAV high-uncertainty containers and switches the UAV’s mode to TRACKING. For each assigned pair, an optimal hover pose is selected on a discrete ring around the target. TRACKING is terminated, and the UAV

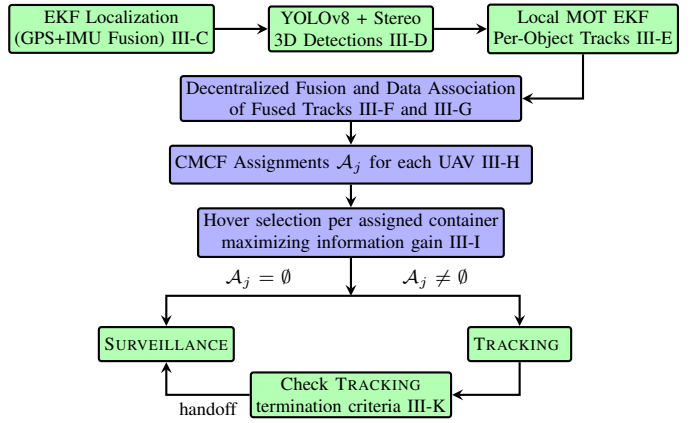


Fig. 1: System-level flow with UAV (green) and Aquabot (blue) ROS nodes.

returns to SURVEILLANCE when the tracked target’s covariance falls below a threshold, or the expected D-optimality gain from any feasible hover pose becomes negligible, ensuring resources focus on the most informative containers.

The proposed method: (i) maintains fully local perception and tracking with only compact state exchange; (ii) performs conservative, correlation-agnostic multi-robot fusion via CI; (iii) supports multiple target assignments tasking with capacities, safety, and stickiness through CMCF; and (iv) explicitly couples assignment with uncertainty-aware view planning for robust tracking.

We first introduce notation and the system overview, then detail localization, detection, tracking, fusion, assignment, hover selection, and mode management. Throughout this paper, UAV (drone) and container (target) are used interchangeably, as they denote the same entities in our context.

A. System Overview and Notation

We consider M UAVs and one Aquabot operating in a shared world frame. Each UAV $j \in \{1, \dots, M\}$ has position $\mathbf{r}_j \in \mathbb{R}^3$. Floating containers are represented as fused 3D tracks indexed by $i \in \{1, \dots, N\}$, with mean $\hat{\mathbf{p}}_i \in \mathbb{R}^3$ and covariance $P_i \in \mathbb{R}^{3 \times 3}$ in the same frame. Bold lowercase symbols denote vectors and uppercase symbols denote matrices. The overall architecture is implemented in ROS as shown in Fig. 1. Each UAV runs a fully onboard perception and tracking stack: an EKF-based self-localization module fusing GPS and IMU into ENU odometry, a YOLOv8 disparity module for 3D detection, and a per-object EKF multi-object tracker with Mahalanobis gating to maintain local obstacle tracks.

Local tracks from all UAVs are combined into fused tracks using conservative covariance intersection, without requiring cross-covariances. The resulting compact fused track arrays are published on a shared ROS topic.

A dedicated assignment node subscribes to the fused tracks and to all UAV odometry topics. It constructs a cost matrix that encodes a per-UAV–target information-gain, UAV–target distance, stickiness to previous assignments, safety-spacing

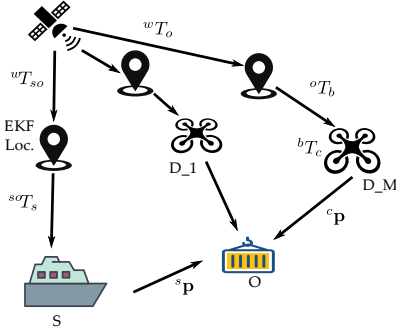


Fig. 2: System TFs Overview.

penalties, and feasibility constraints, and solves a CMCF via successive shortest paths.

Each UAV is issued at least one single *primary* target per allocation cycle. For each assigned UAV-target pair, the node then computes an uncertainty-aware hover pose on a discrete ring and publishes the selected target ID, the hover pose, and the corresponding obstacle state to the downstream navigation components. For each UAV-target pair, the tracking termination criteria are checked, and if satisfied, it enters into SURVEILLANCE mode.

Algorithm 1 summarizes the proposed closed-loop perception-assignment cycle. At each iteration, every UAV reads its current pose r_j and the current fused track set (\hat{p}_i, P_i) . The CMCF problem is then solved to produce assignments $\{\mathcal{A}_j\}$, selecting which targets each UAV should prioritize. If UAV j receives a non-empty assignment, it switches to TRACKING, moves to the selected hover pose q_{j,i^*}^* , and updates the target uncertainty $\log \det P_{i^*}$ and expected information gain ΔJ_{i^*} . When the termination criteria in Sec.III-K are met, the target is marked as done, handed off to the Aquabot, the assignment is cleared, and the UAV returns to SURVEILLANCE; otherwise, it remains in SURVEILLANCE when $\mathcal{A}_j = \emptyset$.

B. Coordinate Frames and Transforms

We compute the detected container position \mathbf{p} in both Aquabot and world coordinates as shown in Figure 2, where ${}^w\mathbf{p} = {}^wT_o {}^oT_b {}^bT_c {}^c\mathbf{p}$. The position ${}^c\mathbf{p}$, ${}^w\mathbf{p} \in \mathbb{R}^3$ is expressed in the camera frame c and world frame w via the body frame b and the odometry frame o respectively. ${}^wT_* \in \mathbb{R}^{4 \times 4}$ denotes the rigid-body homogeneous transformation matrix.

The Aquabot uses a base frame s and a ship odometry frame so . The relation between the vessel base and the world frame is written as ${}^w\mathbf{p} = {}^wT_s {}^s\mathbf{p}$, with ${}^wT_s = {}^wT_{so} {}^{so}T_s$, and the inverse transform ${}^sT_w = ({}^wT_s)^{-1}$. The transforms wT_o for each aerial robot and ${}^wT_{so}$ for the vessel are provided by the EKF based localization modules described in Sec. III-C, while the camera-frame points ${}^c\mathbf{p}$ are produced by the YOLOv8 plus disparity pipeline described in Sec. III-D. All agents share a consistent East–North–Up world frame.

C. Agent Localization via EKF

For each robot, we model the state as $\mathbf{x}_t = [x, y, z, v_x, v_y, v_z, a_x, a_y]^\top$, where (x, y, z) is the posi-

Algorithm 1 Decentralized Perception–Assignment

```

1: while system active do
2:   for each UAV  $j \in \{1, \dots, M\}$  do
3:     Read current pose  $r_j$  and fused tracks  $(\hat{p}_i, P_i)$ 
4:   end for
5:   Solve CMCF for  $\{\mathcal{A}_j\}_{j=1}^M$ 
6:   for each UAV  $j \in \{1, \dots, M\}$  do
7:     if  $\mathcal{A}_j \neq \emptyset$  then
8:        $m_j \leftarrow \text{TRACKING}$ 
9:       Hover near  $q_{j,i^*}^*$  using updated  $(\hat{p}_{i^*}, P_{i^*})$ .
10:      Update  $\log \det P_{i^*}$  and  $\Delta J_{i^*}$ 
11:      if (16) or (17) is satisfied then
12:        Mark  $i^*$  as done
13:        Handoff to ASV, Clear assignment.
14:         $m_j \leftarrow \text{SURVEILLANCE}$ 
15:      end if
16:    else
17:       $m_j \leftarrow \text{SURVEILLANCE}$ 
18:    end if
19:   end for
20: end while

```

tion in the world frame, (v_x, v_y, v_z) are the corresponding linear velocities, and (a_x, a_y) are the horizontal accelerations. The motion model assumes constant acceleration in x and y , and uses inertial measurements to drive vertical motion, with zero-mean process noise.

GPS sensor provides measurements of position, modeled as a linear observation with $H_{\text{gps}} = [I_3 \ 0_{3 \times 5}]$ and covariance R_{gps} . The IMU sensor provides horizontal accelerations (a_x, a_y) after gravity compensation, with $H_{\text{imu}} = [0_{2 \times 6} \ I_2]$ and covariance R_{imu} . The EKF combines these two sensor streams; we initialize the position from the first valid satellite fix, set velocities to zero with large initial covariance, and temporarily increase Q during takeoff and aggressive manoeuvres to remain consistent.

D. YOLOv8 Detection and disparity

a) *YOLOv8 Detection*.: We adopt early fusion [26], [27] where rectified disparity is concatenated with RGB to form a 4-channel input (RGBDis). YOLOv8's first convolution is expanded to 4 input channels and fine-tuned (transfer learning) on 5 container classes and standard YOLO augmentations (mosaic, HSV jitter, flips, random scale). The total training loss \mathcal{L} is

$$\mathcal{L} = \lambda_{\text{box}} \mathcal{L}_{\text{IoU}} + \lambda_{\text{dfl}} \mathcal{L}_{\text{DFL}} + \lambda_{\text{cls}} \mathcal{L}_{\text{BCE}}, \quad (1)$$

Where \mathcal{L}_{IoU} , \mathcal{L}_{DFL} , \mathcal{L}_{BCE} are the bounding-box regression loss, distribution Focal Loss and the binary cross-entropy classification loss respectively over obstacle classes. Where as λ_{box} , λ_{dfl} , and λ_{cls} are non-negative scalar weights that control the relative importance of localization, edge refinement, and classification.

b) *Stereo 3D lifting via disparity*: For each detection k with 2D box $\mathcal{B}_k = (u, v, w, h)$ and confidence s_k , we

estimate a robust disparity \hat{d}_k using a trimmed median over valid pixels in \mathcal{B}_k :

$$\hat{d}_k = \text{median}(\{d_{ij} \in \mathcal{B}_k \mid d_{\min} \leq d_{ij} \leq d_{\max}\}), \quad (2)$$

Metric depth and camera-frame coordinates follow the pin-hole model:

$$Z = \frac{fB}{\hat{d}_k}, \quad X = \frac{(u - c_x)Z}{f}, \quad Y = \frac{(v - c_y)Z}{f}, \quad (3)$$

with intrinsics (f, c_x, c_y) and baseline B . We clamp $Z \in [Z_{\min}, Z_{\max}]$ and discard boxes with insufficient valid disparity support.

E. Multi-Object Tracking with EKF

To maintain persistent identities of detected obstacles over time, each hypothesis is represented by an individual EKF track. For a given track i , we use a constant-velocity state in the ENU frame: $\mathbf{x}_{i,t} = [x_i, y_i, z_i, v_{x,i}, v_{y,i}, v_{z,i}]^\top$. The motion model assumes constant velocity with Gaussian acceleration noise: $\mathbf{x}_{i,t+1} = F \mathbf{x}_{i,t} + \mathbf{w}_t$, with process noise $\mathbf{w}_t \sim \mathcal{N}(0, Q)$ and state transition

$$F = \begin{bmatrix} I_3 & \Delta t I_3 \\ 0_{3 \times 3} & I_3 \end{bmatrix}, \quad (4)$$

Measurements correspond to the 3D container position reconstructed from stereo (Sec. III-D):

$$\mathbf{z}_{k,t} = H \mathbf{x}_{i,t} + \mathbf{v}_t, \quad H = [I_3 \ 0_{3 \times 3}], \quad (5)$$

with measurement noise $\mathbf{v}_t \sim \mathcal{N}(0, R_k)$.

Tracks are initialized when an incoming detection cannot be associated with any existing track (Sec. III-G), using the 3D position and zero initial velocity with large covariance. Tracks are pruned when their covariance grows beyond a threshold (loss of observability) or when they have not received any associated detection for a fixed timeout, preventing proliferation of spurious hypotheses.

F. Decentralized Fusion via Covariance Intersection

Track estimates shared among robots may exhibit *unknown cross-correlations* due to common process models, overlapping observations, and information relaying. Naively fusing such estimates while assuming independence can lead to overconfident covariances and inconsistent filtering. To ensure conservative fusion without requiring cross-covariance terms, we adopt *Covariance Intersection* (CI). Given two Gaussian estimates of the same target position $(\hat{\mathbf{p}}_1, P_1)$ and $(\hat{\mathbf{p}}_2, P_2)$, CI computes

$$P_{\text{CI}}^{-1} = \omega P_1^{-1} + (1 - \omega) P_2^{-1}, \quad \omega \in [0, 1], \quad (6)$$

$$\hat{\mathbf{p}}_{\text{CI}} = P_{\text{CI}}(\omega P_1^{-1} \hat{\mathbf{p}}_1 + (1 - \omega) P_2^{-1} \hat{\mathbf{p}}_2). \quad (7)$$

We choose ω by minimizing a scalar uncertainty criterion (e.g., D-optimality):

$$\omega^* = \arg \min_{\omega \in [0, 1]} \log \det(P_{\text{CI}}(\omega)), \quad (8)$$

and apply the above fusion sequentially when more than two robot estimates are available for the same target.

G. Data Association

Accurate multi-object tracking requires resolving the correspondence between incoming 3D detections and existing tracks. We employ a nearest-neighbor association strategy based on the Mahalanobis distance.

Let $\mathbf{z}_{k,t}$ be a candidate detection at time t and $(\hat{\mathbf{x}}_{i,t|t-1}, P_{i,t|t-1})$ the predicted state and covariance of track i . The squared Mahalanobis distance is

$$d_{ki}^2 = \boldsymbol{\nu}_{ki}^\top S_i^{-1} \boldsymbol{\nu}_{ki}. \quad (9)$$

Where $\boldsymbol{\nu}_{ki}$ and S_i are the innovation and covariance matrices respectively. For each detection, we find the track with the smallest d_{ki}^2 and accept the association if $d_{ki}^2 \leq \tau_{\text{gate}}$, where τ_{gate} is a fixed gating threshold. Unmatched detections spawn new tracks, while tracks that receive no detection in the current frame undergo prediction-only updates and are eventually deleted if they remain unobserved for several cycles. This Mahalanobis nearest neighbor scheme is computationally lightweight, robust to moderate clutter, making it well-suited for real-time multi-obstacle tracking on resource-constrained UAVs.

H. Multi-Target Assignment via Min-Cost Flow

We assign UAVs to tracked containers by solving a *capacitated min-cost flow* problem. The objective is to maximize target coverage while minimizing travel effort, and to favor assignments that are expected to *reduce track uncertainty*.

a) Flow network.: We build a directed graph $G = (V, E)$ with nodes

$$V = \{sr\} \cup \{r_j\}_{j=1}^M \cup \{o_i\}_{i=1}^N \cup \{t\},$$

where sr is a source, t a sink, r_j represents UAV j , and o_i represents target track i . Edges are:

- $sr \rightarrow r_j$ (capacity K , cost 0): UAV j can take up to K targets,
- $r_j \rightarrow o_i$ (capacity 1, cost C_{ji}): assigning target i to UAV j ,
- $o_i \rightarrow t$ (capacity 1, cost 0): each target is assigned to at most one UAV.

We send at most $F = \min\{MK, N\}$ units of flow from sr to t . If the edge $r_j \rightarrow o_i$ carries one unit of flow, then target i is assigned to UAV j .

b) Score an assignment (information gain).: We approximate how useful it would be for UAV j to observe target i from its current pose.

Let the UAV-target distance be

$$d_{ji} = \|\mathbf{r}_j - \hat{\mathbf{p}}_i\|.$$

We use a simple range-dependent measurement noise model:

$$R_{ji} = \sigma^2(d_{ji}) I_3, \quad \sigma(d) = \sigma_0 + k d,$$

and a position measurement model $H = I_3$. If UAV j observes target i , the covariance would approximately update to

$$P_{i|j} = (P_i^{-1} + H^\top R_{ji}^{-1} H)^{-1}.$$

We then define an *information-gain proxy* as the reduction in uncertainty volume:

$$\tilde{\Delta J}_{ji} = \log \det(P_i) - \log \det(P_{i|j}). \quad (10)$$

Large $\tilde{\Delta J}_{ji}$ means UAV j is expected to significantly reduce target i 's uncertainty.

c) *Assignment cost.*: For each candidate pair (j, i) we define the edge cost

$$C_{ji} = -\eta \tilde{\Delta J}_{ji} + \beta d_{ji} - \rho \mathbf{1}[i = i_j^{\text{prev}}] + \gamma \phi_j + \kappa \mathbf{1}[d_{ji} > d_{\max}], \quad (11)$$

βd_{ji} penalizes long travel, ($\rho > 0$) discourages frequent target switching (*stickiness*), i_j^{prev} is UAV j 's previous primary target, ϕ_j penalizes UAVs that are already too close to other UAVs (to encourage spatial separation), the last term assigns a large penalty κ to pairs beyond a maximum range d_{\max} (effectively disallowing them).

d) *Solution and output.*: We solve the min-cost flow with a successive shortest path method in real time. The solution returns, for each UAV j , a set of assigned targets \mathcal{A}_j (up to K).

I. Hover Pose Selection

For each assigned UAV target pair, we compute an uncertainty-aware hover pose $q_{j,i}^*$ using a discrete ring search with a D-optimality score. We sample L viewpoints on a ring of radius r_h and a fixed vertical offset h above the target:

$$q(\psi_\ell) = \hat{p}_i + \begin{bmatrix} r_h \cos \psi_\ell \\ r_h \sin \psi_\ell \\ h \end{bmatrix}, \quad \psi_\ell = \frac{2\pi\ell}{L}, \quad \ell = 0, \dots, L-1. \quad (12)$$

For each feasible viewpoint we approximate a range-dependent measurement model. The per-axis standard deviation is modeled as

$$\sigma(r) = \sigma_0 + k r, \quad (13)$$

where $r = \|q(\psi_\ell) - \hat{p}_i\|$ is the slant range, σ_0 is a base accuracy, and k accounts for degradation with distance. This yields a diagonal covariance $R(q(\psi_\ell)) = \text{diag}(\sigma^2, \sigma^2, \sigma^2)$. Using a linear position measurement model $H = I_3$, we compute the D-optimality gain:

$$\Delta J_i(q(\psi_\ell)) = \log \det P_i - \log \det \left((P_i^{-1} + H^\top R(q(\psi_\ell))^{-1} H)^{-1} \right). \quad (14)$$

To trade information gain against motion effort, we score each candidate as and select

$$q_{j,i}^* = \arg \max_{\psi_\ell \text{ feasible}} \Delta J_i(q(\psi_\ell)). \quad (15)$$

The chosen pose $q_{j,i}^*$ is sent to the planning and navigation controllers for switching to TRACKING mode as explained in the preceding subsections.

J. Surveillance and Tracking

Each UAV operates in SURVEILLANCE or TRACKING modes. With no active assignment, it enters SURVEILLANCE mode and the operator sends target goal positions to the control and navigation servers to reach the desired position.

UAVs switch to TRACKING when an assignment is made as presented in III-H. Each UAV selects the most informative target and the hover pose $q_{j,i}^*$. The TRACKING mode is finished when all the assigned targets are tracked, and the tracking termination criteria are met as described below.

K. Tracking Termination Criteria

After each assignment cycle, we prune “completed” targets from the candidate set. A track is marked done if any of the following holds:

$$\log \det P_i \leq \tau_{\log \det}, \quad (16)$$

$$\max_j \Delta J_i(q_{j,i}^*) \leq \tau_{\Delta J}, \quad (17)$$

The threshold $\tau_{\log \det}$ limits the acceptable uncertainty on a container: once $\log \det P_i$ is small enough, the target is considered well localized. $\tau_{\Delta J}$ is a minimum required information gain: if even the best feasible hover pose yields $\Delta J_i(q_{j,i}^*)$ below this value, further observations are not worth the cost.

IV. SIMULATION RESULTS

The simulations were carried out on ROS2 Jazzy, Ubuntu 24.04 (LTS) on Intel Core i7®, with a system RAM of 32GB and NVIDIA RTX 1000 GPU. The video demonstration¹ and is available.

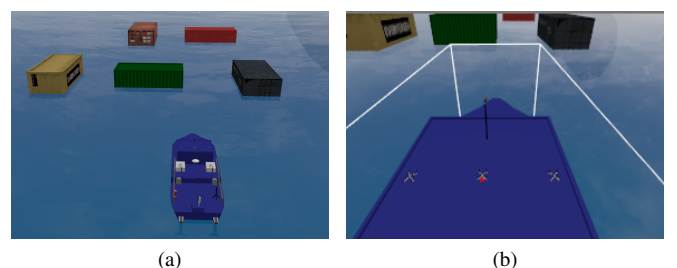


Fig. 3: Initial pos. of (a) Aquabot, containers and (b) drones.

We evaluate the proposed method in Gazebo simulation. We extend the Aquabot environment² by adding three UAVs (*drone 1–drone 3*) and five floating transport containers (C1–C5), each with a standard 20 ft size. The UAVs are equipped with downward-facing RGB stereo cameras, GPS, and IMU sensors, while the Aquabot is equipped with an RGB camera, GPS, and IMU sensors. Fig. 3 shows the simulation environment and the initial positions of the UAVs, the containers, and the Aquabot.

¹https://youtu.be/Vc9aGs_HevA

²<https://github.com/oKermorgant/aquabot>

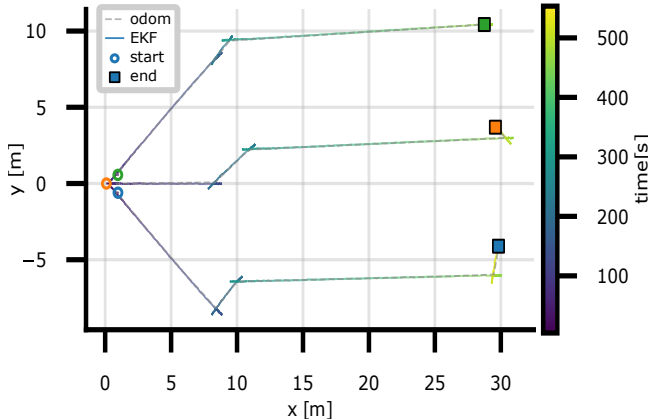


Fig. 4: The mission trajectory, Drone1(blue), Drone2(orange) and Drone3(green).

Fig. 4 reports the UAV trajectories over the full 9-minute experiment, including the initial and final positions. The mission is divided into two phases (*Path 1* and *Path 2*). In *Path 1*, the UAVs take off from the Aquabot in SURVEILLANCE mode, spread out to maximize coverage, and switch to TRACKING when containers are detected and assigned. They then move to the selected hover-ring viewpoints around the targets and, once tracking is completed, return to SURVEILLANCE. In *Path 2*, the UAVs continue along a forward route in SURVEILLANCE mode and again transition to TRACKING whenever assigned containers are detected, moving to the corresponding hover-ring viewpoints before switching back to SURVEILLANCE.

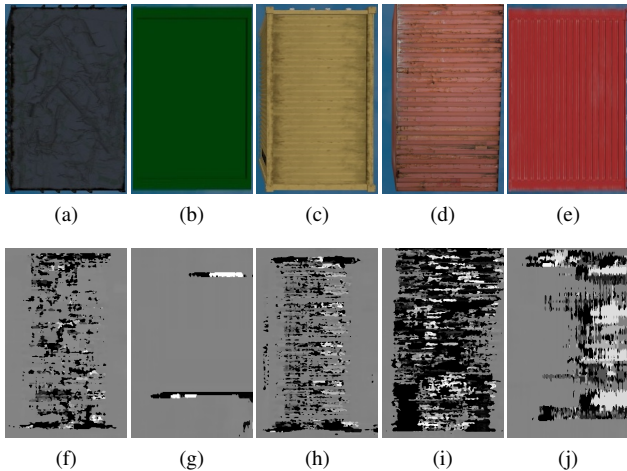


Fig. 5: Containers (C1–C5): RGB images (top row) and disparity images (bottom row).

Finally, Fig. 5 shows representative RGB images and their corresponding disparity maps. The disparity appearance varies across containers due to differences in surface texture, resulting in varying depth contrast and disparity structure within the container regions.

A. Detection

Table I presents a comparative evaluation of the YOLOv8 [28] model and the proposed YOLOv8-RGBDis (our) models trained for container detection. While both models achieve perfect or near-perfect values in precision, recall, and F1-score, the RGBD variant demonstrates consistently higher performance in mAP@0.5 and mAP@0.5:0.95, indicating more reliable detections across various IoU thresholds. Notably, the loss curves of our model exhibit smoother convergence behavior—reflecting improved training stability and optimization. Although the absolute classification metrics are similar, qualitative analysis reveals that our model produces more confident and better-calibrated detections across all container classes, particularly in visually ambiguous or low-contrast conditions. This highlights the utility of incorporating disparity information as an additional input modality to enhance both accuracy and robustness in object detection tasks.

TABLE I: Comparison between models.

Metric	YOLOv8-RGB	Our
mAP@0.5	0.985	0.995
mAP@0.5:0.95	0.952	0.970
Precision	0.998	0.998
Recall	1.000	1.000
F1 Score	1.000	1.000

Fig. 6a shows localization errors over the full mission trajectory for all drones: the median error remains approximately in the range 2.2–4.7 m depending on the container, with the lowest values for C2/C5 (\approx 2.2–2.5 m) and the highest for C4 (\approx 4.3–4.7 m). The spread is moderate (typical interquartile range \approx 0.2–0.4 m), indicating stable measurements despite viewpoint changes along the mission trajectory.

Fig. 6b confirms that detections are high-confidence and well calibrated in most cases: median confidence values are typically \approx 0.93–0.96 across containers and drones, with a small dispersion (IQR \approx 0.005–0.015). Occasional outliers drop to \approx 0.90–0.91, but the bulk of detections remains above \approx 0.93, supporting their use as reliable EKF updates.

Overall, Fig. 6 indicates that the proposed perception front-end provides both accurate 3D geometry and dependable detection confidence for downstream filtering. The bounded meter-level 3D error with tight interquartile ranges suggests that stereo lifting remains stable across drone viewpoints, while the consistently high confidence scores (typically around 0.93–0.96 in median) imply that detections are reliable and not dominated by sporadic failures. Together, these results justify using the detections as regular EKF measurement updates, enabling robust tracking and consistent multi-robot fusion over the full mission.

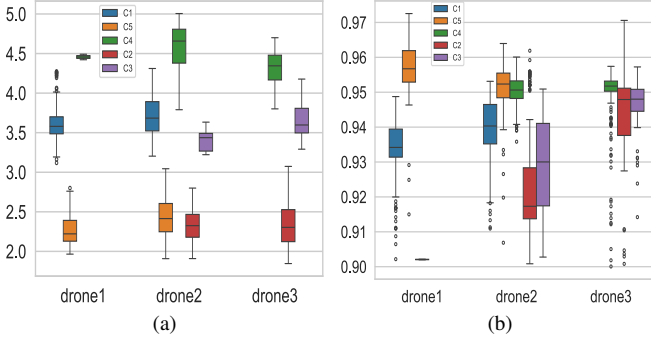


Fig. 6: (a) Detection error (m) and (b) confidence scores of container detections for each drone.

B. Tracking

Figure 7a illustrates the impact of Mahalanobis gating and track management: a large fraction of raw tracks is rejected, while only a compact set of persistent tracks is retained. Across containers, the raw tracks count can reach up to $\approx 2.0 \times 10^3$, whereas the retained (used) set typically remains below $\approx 0.6 \times 10^3$. This corresponds to pruning roughly $\approx 65\%-75\%$ of candidates and keeping only $\approx 25\%-35\%$ as usable tracks (such as C1/C2 on *drone 2* and C2/C3 on *drone 3*). This behavior is desirable in practice because maritime scenes can produce intermittent false positives (e.g., reflections and wakes); without filtering, these would quickly lead to hypothesis explosion and unstable track IDs.

Figure 7b shows that pruning accumulates throughout the mission, indicating continuous suppression of short-lived tracks. *Drone 1*, *drone 2*, and *drone 3* have pruned approximately $\approx 0.9 \times 10^3$, $\approx 1.8 \times 10^3$, and $\approx 1.2 \times 10^3$ hypotheses, respectively, while the global total reaches $\approx 2.2 \times 10^3$. The monotonic, step-like growth reflects repeated rejection of geometrically inconsistent detections, keeping the active track set controlled and stable for fusion and assignment.

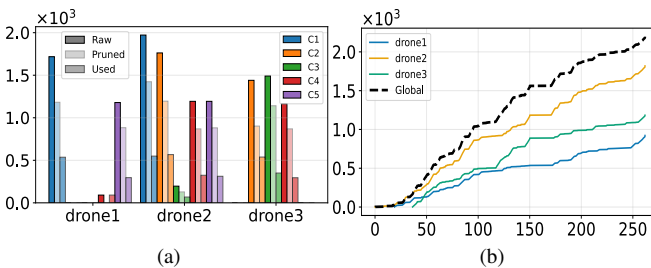


Fig. 7: (a) Raw, pruned, and used tracks per drone; (b) cumulative number of pruned tracks over time (s).

For each drone we define the pruning efficiency as the fraction of raw hypotheses that are rejected:

$$\eta_{\text{prune}}(t) = \frac{N_{\text{pruned}}(t)}{N_{\text{raw}}(t)}, \quad (18)$$

where $N_{\text{raw}}(t)$ is the cumulative number of raw hypotheses generated up to time t , and $N_{\text{pruned}}(t)$ is the cumulative

number rejected by gating. Fig. 8a (Path 1) shows that, after a brief transient, the pruning efficiency converges to $\eta_{\text{prune}} \approx 0.40$ (*drone 1*), 0.37 (*drone 2*), and 0.36 (*drone 3*), i.e., ≈ 0.38 on average. In Path 2 (Fig. 8c), the steady-state values are lower: $\eta_{\text{prune}} \approx 0.26$, 0.23, and 0.17 (mean ≈ 0.22), which is $\approx 41\%$ below Path 1, indicating fewer inconsistent hypotheses to reject.

The raw/pruned counts are consistent with this trend. In Path 1 (Fig. 8b), the cumulative raw track count reaches $\approx 8.6 \times 10^3$ with $\approx 1.6 \times 10^3$ pruned ($\approx 18\%$), leaving $\approx 7.0 \times 10^3$ usable tracks. In Path 2 (Fig. 8d), the raw count reaches $\approx 4.8 \times 10^3$ with $\approx 0.62 \times 10^3$ pruned ($\approx 13\%$), leaving $\approx 4.2 \times 10^3$ usable tracks. Overall, Path 1 contains more short-lived or inconsistent hypotheses, while in both segments, gating keeps the retained track set well controlled for downstream fusion and assignment.

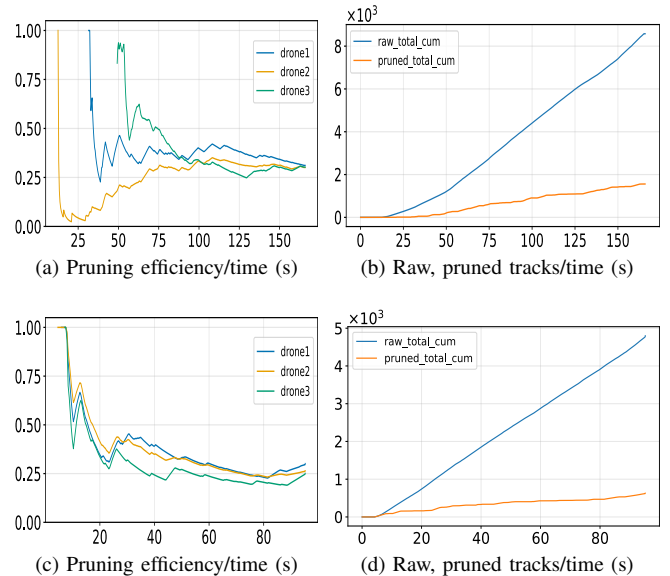


Fig. 8: (a,b) Pruning efficiency and cumulative track evolution for Path 1; (c,d) pruning efficiency and cumulative track evolution for Path 2.

C. Assignment

Fig. 9 summarizes the CMCF assignment described in Section III-H. The first (row 1), second (row 2), and third (row 3) rows show the assigned containers, the XY position error, and the evolution of the information gain, respectively. The columns correspond to *drone 1*, *drone 2*, and *drone 3*. The pink and blue shaded regions indicate SURVEILLANCE and TRACKING modes, respectively. The complete trajectory is divided into Path 1 (0–220 s) and Path 2 (480–600 s).

Row 1 shows the target assignments for each UAV. In Path 1, the allocator assigns containers C1, C2, and C3, while in Path 2 it assigns C5 and C4, with NA indicating no assignment. Notably, in Path 2, *drone 3* receives no target because all available containers are already assigned to other UAVs. Assignments are piecewise constant during TRACKING intervals and return to NA once a target is handed off,

highlighting clear mode switching. Overall, Row 1 illustrates how the allocator actively redistributes UAV attention across targets.

In Row 2, during Path 1 the XY error remains bounded and typically lies in the range $\approx 1.3\text{--}3.4\text{ m}$. In Path 2, *drone 2* shows the largest error when tracking C4 (up to $\approx 3.9\text{ m}$), which contrasts with the corresponding detection error reported in Fig. 6a. In contrast, *drone 1* exhibits a clear reduction in error to $\approx 1.3\text{--}1.6\text{ m}$ when tracking C5, illustrating the benefit of repeated observations from the selected hover viewpoints once the UAV enters the hovering region (Sec. III-I).

Row 3 reports the D-optimality uncertainty measure $\log \det(\cdot)$ of the covariance for each assigned target. The blue curve, $\log \det P$, corresponds to the *predicted* covariance before incorporating a new measurement, whereas the orange curve, $\log \det P^+$, corresponds to the *updated* covariance after the EKF measurement update. In both Path 1 and Path 2, during each TRACKING interval for a given drone-container pair, $\log \det P^+$ consistently drops well below $\log \det P$, showing that each measurement yields a substantial reduction in uncertainty. Overall, this trend confirms that the perception-tracking loop steadily contracts the target covariance once the UAV reaches the selected hovering viewpoint avoiding unnecessary observations when the expected additional information gain becomes marginal.

Overall, Fig. 9 summarizes the UAV-container assignments and their impact on estimation. It shows that assignments during TRACKING, the XY error remains bounded and often decreases after the UAV reaches the hover-ring viewpoint, and the target uncertainty consistently contracts during TRACKING as $\log \det P^+$ drops below $\log \det P$ until termination when further information gain becomes marginal.

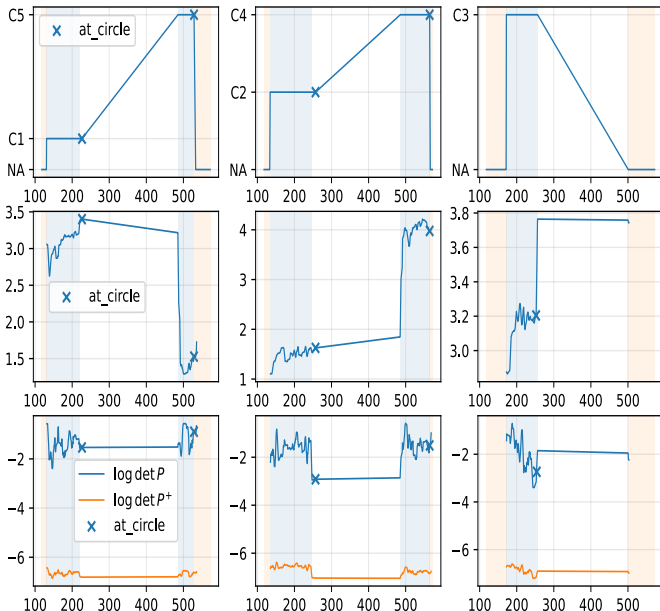


Fig. 9: Assigned containers, position error, and uncertainty propagation of each drone over the full trajectory.

Fig. 10 reports the empirical assignment distribution (fraction of assigned samples) for the entire trajectory. *Drone 1* is assigned primarily to C1 (0.67) and C5 (0.33), with negligible assignments to C2–C4. *Drone 2* splits its assignments between C2 (0.59) and C4 (0.41), while *drone 3* is exclusively assigned to C3 (1.00). Overall, the matrix exhibits a near one-to-one allocation pattern with limited overlap between UAVs, indicating that the allocator effectively partitions the targets and avoids redundant tracking while maintaining full coverage.

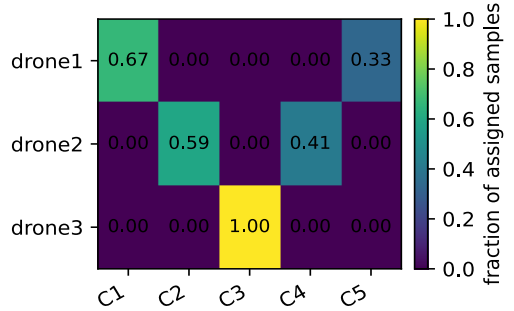


Fig. 10: Drone and container assignment matrix.

Overall, the simulation results validate the proposed decentralized perception-tracking-assignment loop in a realistic maritime scenario. The RGB+disparity perception frontend provides accurate observations despite reflective water effects, enabling reliable EKF updates. Mahalanobis-gated EKF tracking, together with pruning, suppresses short-lived false hypotheses and maintains a compact, stable set of target tracks throughout the mission. Building on these fused tracks, the information-driven CMCF allocator with hovering viewpoint selection consistently directs UAV attention toward the most uncertain containers, which keeps the position error bounded and produces a sustained reduction in covariance.

V. CONCLUSIONS

We presented a decentralized multi-robot framework for maritime container detection and tracking with multiple UAVs and an autonomous surface vessel. The system combines YOLOv8+stereo observations, Mahalanobis-gated EKF tracking, and covariance-intersection fusion, with an information-driven allocator and hovering viewpoint selection. Simulation results show bounded tracking errors and consistent covariance reduction, motivating future validation in real maritime conditions with intermittent communication. Future work will extend the system towards real-world experiments in outdoor maritime environments, addressing challenges such as dynamic water surfaces, communication dropouts [29], and on-board resource constraints. Moreover, we plan to integrate semantic understanding (e.g., classifying container types) and explore advanced decentralized optimization methods for large-scale multi-robot deployments.

ACKNOWLEDGMENT

This work was conducted within the framework of the NExT Senior Talent Chair DeepCoSLAM, funded by the

French Government through the program "Investments for the Future" administered by the National Agency for Research (ANR-16-IDEX-0007). We also extend our gratitude to the Région Pays de la Loire and Nantes Métropole for their invaluable support in facilitating this research endeavour.

REFERENCES

- [1] L. Paull, S. Saeedi, M. Seto, and H. Li, "Auv navigation and localization: A review," *IEEE Journal of Oceanic Engineering*, vol. 39, no. 1, pp. 131–149, 2014.
- [2] M.-Q. Dao, J. S. Berrio, V. Frémont, M. Shan, E. Héry, and S. Worrall, "Practical collaborative perception: A framework for asynchronous and multi-agent 3d object detection," *IEEE Transactions on Intelligent Transportation Systems*, vol. 25, no. 9, pp. 12 163–12 175, 2024.
- [3] W. Geng, J. Yi, and L. Cheng, "An efficient detector for maritime search and rescue object based on unmanned aerial vehicle images," *Displays*, vol. 87, p. 102994, 2025.
- [4] R. Douguet, D. Heller, and J. Laurent, "Multimodal perception for obstacle detection for flying boats - unmanned surface vehicle (usv)," in *OCEANS 2023 - Limerick*, 2023, pp. 1–8.
- [5] V. Varga, B. Kiefer, M. Messmer, and A. Zell, "Seadronesee: A maritime benchmark for detecting humans in open water," in *IEEE/CVF Winter Conference on Applications of Computer Vision (WACV)*, 2022.
- [6] Maritime Computer Vision Initiative, "The maritime computer vision initiative: Seadronesee and related challenges," in *IEEE/CVF Conference on Computer Vision and Pattern Recognition Workshops (CVPRW)*, 2023.
- [7] D. Nunes, J. Fortuna, B. Damas, and R. Ventura, "Real-time vision based obstacle detection in maritime environments," in *2022 IEEE International Conference on Autonomous Robot Systems and Competitions (ICARSC)*, 2022, pp. 243–248.
- [8] Y. Zhang, Q. Tao, and Y. Yin, "A lightweight man-overboard detection and tracking model using aerial images for maritime search and rescue," *Remote Sensing*, vol. 16, no. 1, 2024.
- [9] Z. Li *et al.*, "Practical stereo matching via cascaded recurrent network with adaptive correlation," in *IEEE/CVF Conference on Computer Vision and Pattern Recognition (CVPR)*, 2022.
- [10] Y. Zhang *et al.*, "Bot-sort: Robust associations in tracking-by-detection," in *European Conference on Computer Vision (ECCV)*, 2022.
- [11] X. Weng, J. Wang, D. Held, and M. Hebert, "3d multi-object tracking: A baseline and new evaluation metrics," in *2020 IEEE/RSJ International Conference on Intelligent Robots and Systems (IROS)*, 2020.
- [12] Z. Shao, Y. Yin, H. Lyu, and C. Guedes Soares, "A robust method for multi object tracking in autonomous ship navigation systems," *Ocean Engineering*, vol. 311, p. 118560, Nov. 2024.
- [13] A. B. Bakht, H. Javed *et al.*, "Mvtd: A benchmark for maritime visual object tracking," *arXiv preprint*, 2025.
- [14] Y. Zhou, Y. Liu, P. Zhu, and X. Wang, "Distributed invariant kalman filter for cooperative localization using matrix lie groups," *arXiv preprint*, 2024.
- [15] T.-K. Chang, K. Chen, and A. Mehta, "Resilient and consistent multi-robot cooperative localization with covariance intersection," *arXiv preprint*, 2021.
- [16] S. Dong, R. Lin, W.-W. Zhao, and Y.-H. Cheng, "Robot global relocalization based on multi-sensor data fusion," in *2022 2nd International Conference on Robotics, Automation and Artificial Intelligence (RAAI)*, 2022, pp. 35–42.
- [17] S. J. Julier and J. K. Uhlmann, "A non-divergent estimation algorithm in the presence of unknown correlations," in *Proceedings of the American Control Conference (ACC)*, 1997, pp. 2369–2373.
- [18] H. Chakraa, F. Guérin, E. Leclercq, and D. Lefebvre, "Optimization techniques for multi-robot task allocation problems: Review on the state-of-the-art, challenges and new directions," *Robotics and Autonomous Systems*, vol. 168, p. 104492, 2023.
- [19] A. Freitas, E. Nunes, C. Tovey, and M. Gombolay, "Smt-based dynamic multi-robot task allocation," *Georgia Institute of Technology, Tech. Rep. GIT-IRIM-TR-24-009*, 2024.
- [20] A. Gab, S. Guy, and N. Agmon, "Multi-robot task allocation with ordinal rewards," in *Proceedings of the International Conference on Autonomous Agents and Multiagent Systems (AAMAS)*, 2025.
- [21] O. T. Arnegard, F. S. Leira, H. H. Helgesen, S. Kemna, and T. A. Johansen, "Detection of objects on the ocean surface from a uav with visual and thermal cameras: A machine learning approach," in *2021 International Conference on Unmanned Aircraft Systems (ICUAS)*, 2021, pp. 81–90.
- [22] J. Wang, Y. Cheng, Q. Zhang *et al.*, "Sr-detr: Target detection in maritime rescue scenarios from uav platforms," *Remote Sensing*, vol. 17, no. 8, p. 1297, 2025.
- [23] N. Wojke, A. Bewley, and D. Paulus, "Simple online and realtime tracking with a deep association metric," in *2017 IEEE International Conference on Image Processing (ICIP)*, 2017, pp. 3645–3649.
- [24] W. Wu, Q. Li, Z. Hu, and M. H. Meng, "Guaranteeing consistency in the fusion of correlated gaussian estimates," *IEEE Transactions on Automatic Control*, vol. 63, no. 3, pp. 619–629, 2018.
- [25] C. Tu, X. Cui, G. Liu, and M. Lu, "Weighted covariance intersection for range-based distributed cooperative localization of multi-agent systems," *arXiv preprint*, 2025.
- [26] B. Wang, Z. Zhang, J. Li, S. Chen, Y. Qiao, and Z. Liu, "Adversarial robustness of deep sensor fusion models," in *Proceedings of the*

IEEE/CVF Winter Conference on Applications of Computer Vision (WACV), 2022, pp. 3619–3627.

- [27] T. Ophoff, K. Van Beeck, and T. Goedemé, “Exploring rgb+depth fusion for real-time object detection,” *Sensors*, vol. 19, no. 4, p. 866, 2019.
- [28] R. Varghese and S. M., “Yolov8: A novel object detection algorithm with enhanced performance and robustness,” in *2024 International Conference on Advances in Data Engineering and Intelligent Computing Systems (ADICS)*, 2024, pp. 1–6.
- [29] H. Kim, A. James, A. Seth, E. Kuantama, J. Williamson, Y. Feng, and R. Han, “Continuous marine tracking via autonomous uav handoff,” 2025.